

# Evaluations of uncertainties in simulations of propagation of ultrahigh-energy cosmic-ray nuclei derived from microscopic nuclear models

E. Kido<sup>a</sup>, T. Inakura<sup>b</sup>, M. Kimura<sup>c</sup>, N. Kobayashi<sup>d</sup>, S. Nagataki<sup>a,e</sup>,  
N. Shimizu<sup>f</sup>, A. Tamii<sup>d</sup>, Y. Utsuno<sup>g</sup>

<sup>a</sup>*RIKEN Cluster for Pioneering Research,  
Astrophysical Big Bang Laboratory (ABBL), Wako, Saitama, Japan*

<sup>b</sup>*Laboratory for Zero-Carbon Energy, Tokyo Institute of Technology,  
Meguro, Tokyo, Japan*

<sup>c</sup>*Hokkaido University,*

*Sapporo, Hokkaido, Japan*

<sup>d</sup>*Research Center for Nuclear Physics, Osaka University,  
Ibaraki, Osaka, Japan*

<sup>e</sup>*RIKEN Interdisciplinary Theoretical and Mathematical Sciences Program (iTHEMS),  
Wako, Saitama, Japan*

<sup>f</sup>*Center for Computational Sciences, University of Tsukuba,  
Tsukuba, Ibaraki, Japan*

<sup>g</sup>*Japan Atomic Energy Agency,  
Tokai, Ibaraki, Japan*

---

## Abstract

Photodisintegration is a main energy loss process of ultrahigh-energy cosmic-ray (UHECR) nuclei in intergalactic space at the highest energies. Therefore, it is crucial to understand photodisintegration's systematic uncertainty to simulate the propagation of UHECR nuclei. In this work, we calculated the cross sections using the random phase approximation (RPA) of density functional theory (DFT), a microscopic nuclear model. We calculated the  $E1$  strength of 29 nuclei using three different density functionals. We obtained the cross sections of photonuclear reactions, including photodisintegration, with the  $E1$  strength. Then, we implemented the cross sections in a cosmic ray propagation code CRPropa. We found that the difference between the RPA calculations and TALYS in CRPropa in the energy spectrum can be more than the statistical uncertainty of UHECR energy spectrum assuming some astrophysical parameters. We also found that the difference of some astrophysical parameters obtained by a combined fit of UHECR energy spec-

trum and composition data can be more than the uncertainty of the data between the RPA calculations and TALYS assuming a phenomenological model of UHECR sources.

*Keywords:* ultra high energy cosmic rays, cosmic ray theory

---

## 1. Introduction

Observations of ultrahigh-energy cosmic rays (UHECRs) recently showed implications that some extragalactic sources emit atomic nuclei at the highest energies. The energy dependence of the mean values of the slant depth at the shower maximum  $\langle X_{\max} \rangle$ , which the Pierre Auger Observatory [1] detected, is not compatible with the expectation of pure protons or pure irons when three hadron interaction models tuned to the LHC data are used [2]. The result implied that the composition of UHECRs becomes lighter up to  $10^{18.27}$  eV and heavier above that energy. The contribution of light nuclei between proton and iron was needed to interpret the observed distribution of the  $X_{\max}$  [3]. A significant dipole amplitude of a large-scale anisotropy in the arrival directions of UHECRs was discovered by the Pierre Auger Collaboration, and the direction of the dipole implied the source distribution in the local large-scale structure [4]. Some evidence of the correlation between the arrival directions of UHECRs and extragalactic sources was detected by the Pierre Auger Observatory [5] and by a working group [6] of Auger and Telescope Array [7].

The experimental evidence induces motivation to study light nuclei which were emitted from extragalactic sources. To constrain astrophysical parameters such as the power index of the injection spectrum and acceleration limit of possible extragalactic sources, fitting observables such as energy spectrum and  $X_{\max}$  using simulations of propagation of UHECR nuclei in intergalactic space is useful. The most critical interactions of the nuclei at the highest energies are photonuclear reactions with cosmic microwave background (CMB) photons. The average energy of a CMB photon is  $6.3 \times 10^{-4}$  eV today. The energies of CMB photons reach a few tens of MeV in the rest frame of UHECR nuclei with Lorentz factors greater than approximately  $10^9$ . If a photon with a few tens of MeV in a nucleus's rest frame is absorbed by the nucleus, the nucleus is excited by the photon. Accelerator experiments measured the photonuclear reactions in the laboratories. The electric dipole ( $E1$ ) excitation is the dominant component of the excitation. There are large

peaks known as giant dipole resonances (GDRs) at approximately 20 MeV in the cross sections, and the GDRs are dominant in the  $E1$  excitation. The excited nucleus loses the energy by emitting  $p$ ,  $n$ ,  $\alpha$ ,  $\gamma$  particles and so on. The impact of the GDRs on UHECR nuclei can be found in the right figure in Fig. 3 in [8], for example.

However, the cross sections of photonuclear reactions often suffer from systematic discrepancies among different experimental methods at different accelerator facilities. In the extreme case shown in [9], there were about 100% systematic differences in the neutron emitting cross sections of 19 nuclei between the measurements in Livermore and Saclay. There is also a lack of measurements of many elements as visualized in [10]. Furthermore, the cross sections of light nuclei are difficult for nuclear theories to describe accurately because individual nuclei manifest their own complicated aspects of nuclear structure, e.g., shell structure, deformation, and  $\alpha$  cluster structure. Solving these issues in both experiments and theories is one of the main motivations of the Photo-Absorption of Nuclei and Decay Observation for Reactions in Astrophysics (PANDORA) project [11, 12]. Three facilities in Japan, Romania, and South Africa plan to measure photoabsorption cross sections and neutron, proton,  $\alpha$ , and  $\gamma$  decays from light to  $A \sim 60$  nuclei systematically in this project with modern experimental methods of virtual-photon excitation by proton scattering [13] and real-photon excitation by a high-intensity laser-Compton scattering gamma-ray beam [14]. This project will test the consistency among three facilities ensuring the mutual consistency through measurements on  $^{27}\text{Al}$  target.

The Puget-Stecker-Bredenkamp (PSB) model [15], which implements a single decay chain of each nucleus, was widely used. In [16], to implement multiple decay chains was recommended for the simulations of UHECRs at energies around  $10^{21}$  eV by showing the calculations with TALYS [17]. TALYS is generally used to calculate photonuclear reactions in several propagation codes of UHECRs, e.g., CRPropa [18], SimProp [19], and PRINCE [20]. TALYS can include  $E1$  strength functions which are directly converted to the cross sections used in these propagation codes. If no data of  $E1$  strength is included in TALYS, these cross sections are calculated using the phenomenological empirical laws; The peak energy of the cross sections is given as  $31.2A^{-1/3} + 20.6A^{-1/6}$  MeV. It is known that this empirical law overestimates the peak energy in light nuclei, while it provides reasonable values for heavy nuclei. For some nuclei (nine nuclei in light nuclei to  $A \sim 60$ ), peak energies that are evaluated from the experimental data are used for the cal-

culations. Otherwise, the empirical laws are used. Also nuclear deformation affects the cross section. The deformation splits the cross section distribution to two-peak structure and shifts the peak energy by 1-2 MeV from one in the spherical case. This effect is not taken in the empirical law. The cross sections calculated by TALYS have non-negligible uncertainties. Therefore, the propagation codes mainly use the current experimental data for  $E1$  strength functions of TALYS.

The PANDORA project plans to measure a few nuclei in a few years and finally measure a few dozens of important nuclei for systematically evaluating and improving the model predictions. The photonuclear reactions will be predicted by the models for the rest of the nuclei relevant to the UHECR propagation. Therefore, the reliable nuclear model prediction is indispensable for the project and would also be informative to interpret the current experimental data. In this work, we calculated the cross sections within the random phase approximation (RPA) of nuclear-density functional theory (DFT) [21, 22]. The RPA calculations have systematic uncertainty, which is not known well and discussed in Section 5. The experimental data also has systematic uncertainty, as introduced in this section. We found that there is a systematic difference between the experimental data and the RPA calculations for  $E1$  strength, which is shown in Section 3. In this study, we demonstrated how the uncertainties affect the resulting UHECR energy spectra and compositions. The uncertainties will be studied in both theoretical and experimental ways.

In Section 2, we explain how we calculated the  $E1$  strength functions with RPA and how we simulated propagation of UHECR nuclei using CRPropa 3 [18]. In Section 3, the photoabsorption cross sections obtained by the RPA calculations are compared with the cross sections obtained using previous experimental data. The difference of simulated UHECR energy spectra and compositions when photonuclear reactions in CRPropa 3 are replaced with the results of the RPA calculations is shown in Section 4. In the later sections, we often describe simulations using CRPropa 3 with the default settings as "TALYS" to be distinguished from the RPA calculations. We describe simulations with the RPA calculations as "Skyrme-RPA" in this paper. We also compared astrophysical parameters, which were obtained by fitting the results of the Auger Collaboration with TALYS and Skyrme-RPA. The contributions and influences of individual nuclei are discussed in Section 4. Finally, the obtained results are summarized, and the systematic uncertainty is discussed in Section 5.

## 2. Method

We applied the RPA to obtain the  $E1$  strength function in the following way. The RPA equation is derived as small amplitude limit of the time-dependent density functional theory [23, 24]. Under a weak, time-dependent external field  $V_{ext}(t)$ , the transition density  $\delta\rho(t)$ , which describes the density fluctuation from the ground-state density  $\rho_0$ , follows the equation

$$i\frac{d}{dt}\delta\rho(t) = [h_0, \delta\rho(t)] + [V_{ext}(t) + \delta h(t), \rho_0] , \quad (1)$$

where  $h_0 = h[\rho_0]$  is the single-particle Hamiltonian. The residual field  $\delta h(t)$  is induced by density fluctuation,  $h[\rho_0 + \delta\rho(t)] = h_0 + \delta h(t)$ . Assuming that  $\delta\rho(t)$ ,  $V_{ext}(t)$ , and  $\delta h(t)$  oscillate with a frequency  $\omega$  as  $\delta\rho(t) = \delta\rho(\omega)e^{-i\omega t} + \delta\rho^\dagger(\omega)e^{i\omega t}$ , Eq. (1) is recast to

$$\omega\delta\rho(\omega) = [h_0, \delta\rho(\omega)] + [V_{ext}(t) + \delta h(\omega), \rho_0] . \quad (2)$$

The residual field  $\delta h(\omega)$  is calculated by the functional derivative of single-particle hamiltonian with respect to the density,  $\delta h = \partial h / \partial \rho \cdot \delta \rho$ . Because  $\delta\rho(\omega)$  is not necessarily Hermitian, we introduce forward and backward amplitudes,  $|X_i(\omega)\rangle$  and  $|Y_i(\omega)\rangle$ , to express the transition density  $\delta\rho(\omega)$ ,

$$\delta\rho(\omega) = \sum_{i=1}^A \{|X_i(\omega)\rangle\langle\phi_i| + |\phi_i\rangle\langle Y_i(\omega)|\} , \quad (3)$$

where  $A = N + Z$  is the mass number of a nucleus, and  $|\phi_i\rangle$  are the occupied orbitals in the ground state,  $h_0|\phi_i\rangle = \epsilon_i|\phi_i\rangle$  ( $i = 1, 2, \dots, A$ ). Substituting this into Eq. (2), we obtain the RPA equations:

$$\omega|X_i(\omega)\rangle = (h_0 - \epsilon_i)|X_i(\omega)\rangle + \{V_{ext}(t) + \delta h(\omega)\}|\phi_i\rangle , \quad (4)$$

$$-\omega\langle Y_i(\omega)| = \langle Y_i(\omega)| (h_0 - \epsilon_i) + \langle\phi_i| \{V_{ext}(t) + \delta h^\dagger(\omega)\} . \quad (5)$$

In our implementation, we employ the grid representation of the three-dimensional Cartesian-coordinate space.

To calculate the continuous strength function for a given one-body operator  $F$ , we adopt an external field of  $V_{ext}(t) = Fe^{-i\omega t} + F^\dagger e^{i\omega t}$ . Then, the discretized transition strength is expressed with the forward and backward

amplitudes,

$$\begin{aligned}
S(E; F) &\equiv \sum_n |\langle n|F|0\rangle|^2 \delta(E - E_n) \\
&= -\frac{1}{\pi} \text{Im} \sum_i \{ \langle \phi_i|F|X_i(\omega)\rangle + \langle Y_i(\omega)|F^\dagger|\phi_i\rangle \} \quad (6)
\end{aligned}$$

for a real frequency  $\omega = E$ . Here,  $|n\rangle$  are energy eigenstates of the total system. Since the transition strength is continuous above the nucleon decay energy, we introduce complex frequencies with a finite imaginary part,  $\omega = E + i\gamma/2$ .  $\gamma$  describes the spreading width of the GDR and we adopt  $\gamma = 2.0$  MeV. The transition strength becomes

$$S(E; F) = \frac{\gamma}{2\pi} \sum_n \left\{ \frac{|\langle n|F|0\rangle|^2}{(E - E_n)^2 + (\gamma/2)^2} - \frac{|\langle n|F^\dagger|0\rangle|^2}{(E + E_n)^2 + (\gamma/2)^2} \right\} \quad (7)$$

For the dipole case, we consider an electric dipole operator for  $F$ :

$$F = D_z = \frac{N}{A} e \sum_{p=1}^Z z_p - \frac{Z}{A} e \sum_{n=1}^N z_n, \quad (8)$$

and similar operators for  $D_x$  and  $D_y$ . The photoabsorption cross section is given as

$$\sigma(E) = \frac{4\pi^2 E}{3c} \sum_{\mu=x,y,z} S(E; D_\mu). \quad (9)$$

We used three parameter sets of the Skyrme energy-density functional, SkM\* [25], SLy4 [26], and UNEDF1 [27]. SkM\* is one of the commonly used Skyrme functionals for nuclear structure calculations. SLy4 is constructed to reproduce the equation of state of infinite nuclear matter proposed by [28] as well as experimental data of binding energies and radii in a wide mass region, especially in neutron-rich nuclei. UNEDF1 is recently designed as a sophisticated version of Skyrme parameter set. For nuclei with odd-neutron and/or odd-proton numbers, we employ the filling approximation [29]. Table 1 lists the one nucleon separation energies applied in the calculations.

We used the  $E1$  strength function up to 200 MeV obtained from the RPA calculations as an input to the version 1.96 of the TALYS code. Other parameters of TALYS such as quasi-deuteron component and giant quadrupole

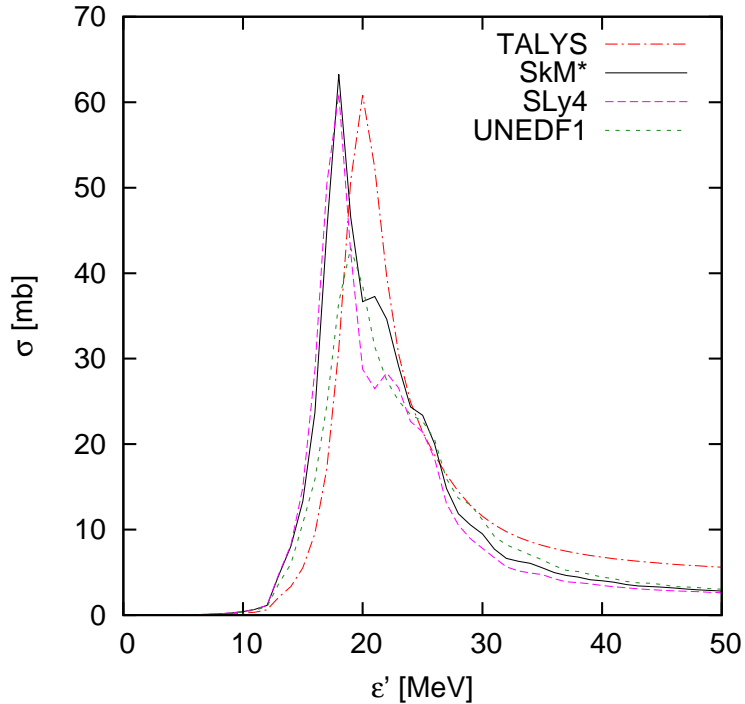


Figure 1: Comparison of nonelastic cross sections of  $^{28}\text{Si}$  of TALYS-1.96 using  $E1$  strength functions of experimental data and models.  $\epsilon'$  denotes photon energy in the nucleus' rest frame. The cross sections at  $\epsilon' = 1, 2, 3 \dots 200$  MeV were discretely calculated and plotted with lines. The red dash-dotted line was calculated using the  $E1$  strength function with the parameters of the experimental data in Table 2 of CRPropa 3 [18]. The black solid, pink long dashed, and forest green dashed lines were derived from the  $E1$  strength functions which were calculated using the RPA calculations with different density functionals.

resonances are set to the default values. We obtained nonelastic cross sections as outputs of TALYS. Fig. 1 shows the nonelastic cross sections of  $^{28}\text{Si}$  calculated using different functionals. The difference of the peak energies and cross sections in this figure mainly affect propagation of UHECR nuclei. We repeated this procedure for 29 stable nuclei ( $^{10}\text{B}$ ,  $^{11}\text{B}$ ,  $^{12}\text{C}$ ,  $^{13}\text{C}$ ,  $^{14}\text{N}$ ,  $^{15}\text{N}$ ,  $^{16}\text{O}$ ,  $^{17}\text{O}$ ,  $^{18}\text{O}$ ,  $^{19}\text{F}$ ,  $^{20}\text{Ne}$ ,  $^{21}\text{Ne}$ ,  $^{22}\text{Ne}$ ,  $^{23}\text{Na}$ ,  $^{24}\text{Mg}$ ,  $^{25}\text{Mg}$ ,  $^{26}\text{Mg}$ ,  $^{27}\text{Al}$ ,  $^{28}\text{Si}$ ,  $^{32}\text{S}$ ,  $^{36}\text{Ar}$ ,  $^{40}\text{Ca}$ ,  $^{48}\text{Ti}$ ,  $^{51}\text{V}$ ,  $^{52}\text{Cr}$ ,  $^{53}\text{Cr}$ ,  $^{54}\text{Cr}$ ,  $^{55}\text{Mn}$  and  $^{56}\text{Fe}$ ). Fig. 2 shows a chart of nuclear species where the 29 nuclei are highlighted. Many of these 29 nuclei are expected to be in the decay chain of primary nuclei such as  $^{14}\text{N}$ ,  $^{28}\text{Si}$ , and  $^{56}\text{Fe}$ , which are often assumed in the propagation of UHECR nuclei in intergalactic space.

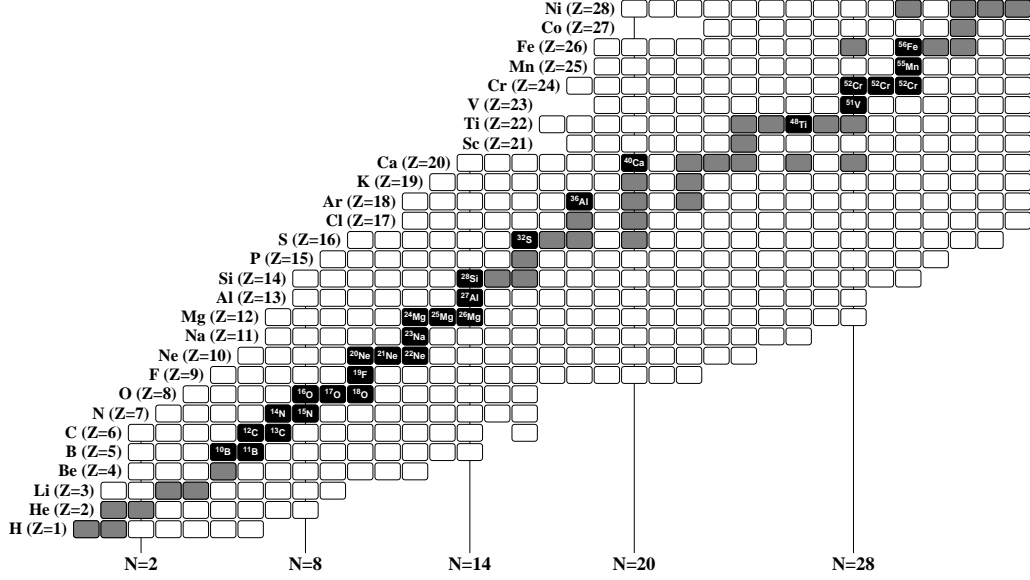


Figure 2: A chart of nuclear species. The horizontal axis represents the number of neutrons, and the vertical axis represents the number of protons. Gray or black boxes show stable nuclei. The 29 black boxes show nuclei that we considered in this work.

The integral of the nonelastic cross sections with background photons to calculate the reaction rates is given as

$$\lambda^{-1}(\Gamma, z) = \frac{1}{2\Gamma^2} \int_0^\infty \int_0^{2\Gamma\epsilon} n(\epsilon, z) \frac{1}{\epsilon^2} \epsilon' \sigma(\epsilon') d\epsilon' d\epsilon, \quad (10)$$

where  $n$  is the spectral number density of background photons,  $\Gamma$  is the Lorentz factor of the nucleus,  $\epsilon$  is the photon energy,  $z$  is the redshift,  $\epsilon' = \Gamma\epsilon(1 - \cos\theta)$  shows the photon energy in the nucleus' rest frame,  $\theta$  is the opening angle between the photon and the nucleus momenta,  $\sigma$  shows the nonelastic cross section and  $\lambda$  represents the mean free path. This formula was shown as Eq. (4) in [30]. The differential coefficient of Eq. (10) can be given by

$$\frac{d\lambda^{-1}(\Gamma, z)}{d\epsilon'} = \sigma(\epsilon') \frac{\epsilon'}{2\Gamma^2} \int_{\frac{\epsilon'}{2\Gamma}}^\infty \frac{n(\epsilon, z)}{\epsilon^2} d\epsilon. \quad (11)$$

We used this formula to illustrate the impact of the nonelastic cross sections and background photon energy spectrum on the reaction rates. Fig. 3 and Fig. 4 show the integral of the photon spectrum in the right formula of



Eq. (11) and the differential coefficient  $d\lambda^{-1}(\Gamma, z)/d\epsilon'$ , respectively. A summary of the nonelastic cross sections and the mean free paths is shown in Section 3.

We simulated the energy spectra and compositions of UHECR nuclei on the earth using CRPropa 3 and fitted the results of the Auger Collaboration. We assumed the following things in the simulations. There are identical UHECR sources distributed in the universe, which emit five nuclei, i.e.,  $^1\text{H}$ ,  $^4\text{He}$ ,  $^{14}\text{N}$ ,  $^{28}\text{Si}$ , and  $^{56}\text{Fe}$ . The injection energy spectrum of these nuclei is described by

$$\frac{dN}{dE} = C f_A \left( \frac{E}{10^{18}\text{eV}} \right)^{-p} f_{\text{cut}}(E, ZR_{\text{cut}}), \quad (12)$$

where  $C$  is the normalization constant,  $f_A$  is the relative fraction of the nucleus,  $p$  is the power index of the energy spectrum and  $f_{\text{cut}}(E, ZR_{\text{cut}})$  is given by

$$f_{\text{cut}}(E, ZR_{\text{cut}}) = \begin{cases} 1, & E < ZR_{\text{cut}} \\ \exp(1 - E/ZR_{\text{cut}}), & E \geq ZR_{\text{cut}} \end{cases} \quad (13)$$

where  $R_{\text{cut}}$  denotes the cutoff rigidity. The evolution of the number of sources is  $(1+z)^m$  in the comoving unit volume. [31] is used as the infrared background model. Magnetic fields are small enough to consider one-dimensional cosmic ray propagation from extragalactic sources to the earth. In the simulations, the step sizes of  $p$ ,  $\log(R_{\text{cut}})$  and  $m$  are set to be 0.1, 0.1 and 1, respectively. The minimum value of  $m$  is set to be 0.

We took  $C$ ,  $f_A$  of five nuclei,  $p$ ,  $R_{\text{cut}}$ ,  $m$ , and the energy scale as free parameters. We used 15 data points of the energy spectrum, 10 data points of  $\langle \ln A \rangle$  and 10 data points of  $\sigma^2(\ln A)$  above  $10^{18.7}$  eV for fitting assuming one of the hadron interaction models, SIBYLL-2.3c [32] for simplicity. The energy range  $E > 10^{18.7}$  is the same as the previous studies [20, 33]. In fitting the energy spectrum and  $\sigma^2(\ln A)$ , we considered only the error bars of statistical uncertainties as Gaussian errors. We searched the energy scale as one of the fitting parameters within 14% systematic uncertainty of the Pierre Auger Observatory. In fitting  $\langle \ln A \rangle$ , we considered the systematic uncertainty of each data point instead of statistical uncertainty as a Gaussian error because the systematic uncertainties of most of the data points are much larger than the statistical errors. Then, we replaced the reaction rates of 29 nuclei with the calculated ones using the RPA calculations in CRPropa 3, simulated the propagation of UHECR nuclei, and repeated the fittings.

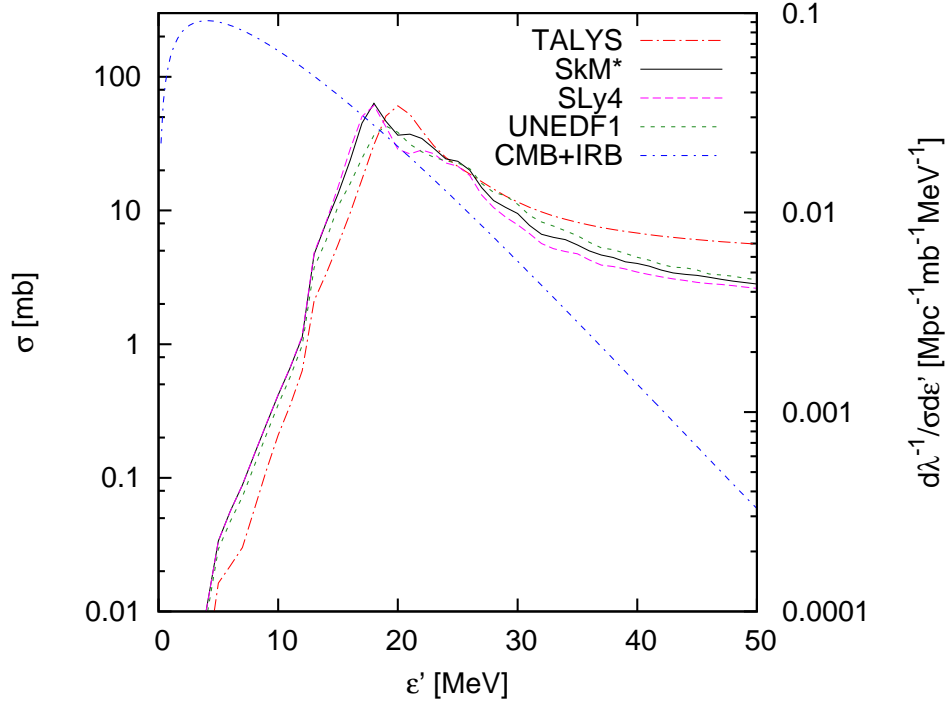


Figure 3: The red dash-dotted, black solid, pink long dashed, and forest green dashed lines show the nonelastic cross sections of  $^{28}\text{Si}$  in Fig. 1 using logarithmic scales. The left vertical axis shows the cross section.  $\epsilon'$  shows photon energy in the nucleus's rest frame. The blue dash-dotted line denotes the differential coefficients of the reaction rates  $d\lambda^{-1}/d\epsilon'$  of  $^{28}\text{Si}$  with  $E = 10^{20.5}$  eV divided by the nonelastic cross sections  $\sigma$ . The right vertical axis shows the scale of the blue line. The blue line was obtained using the cosmic microwave background (CMB) photons, infrared background (IRB) photons [31] and the Lorentz factor of  $^{28}\text{Si}$ . The differential coefficients of the reaction rates in Fig. 4 can be obtained by multiplying the blue line with nonelastic cross sections of  $^{28}\text{Si}$ .

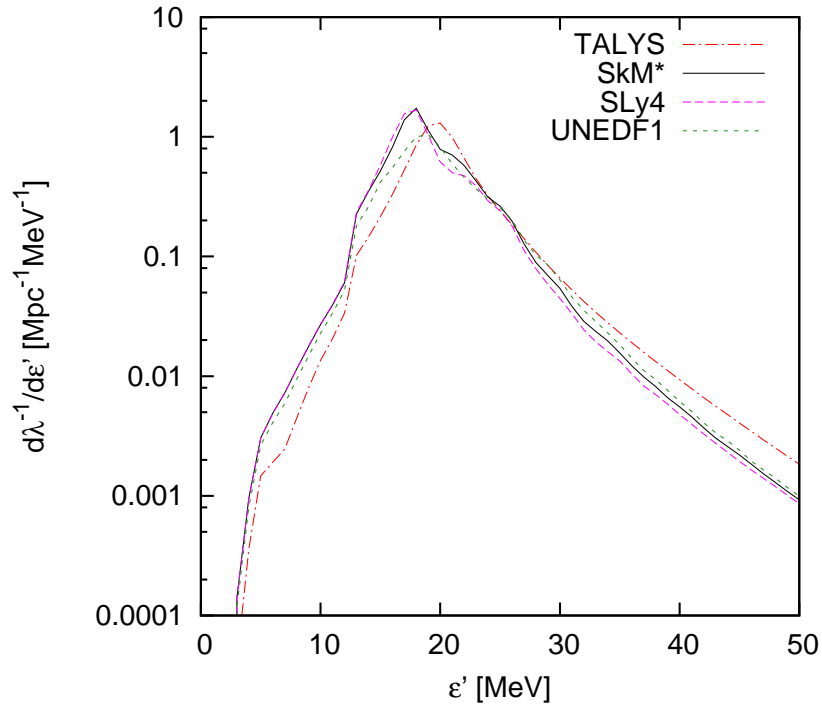


Figure 4: The differential coefficients of the reaction rates  $d\lambda^{-1}/d\epsilon'$  of  $^{28}\text{Si}$  with  $E = 10^{20.5}$  eV obtained by multiplying nonelastic cross sections  $\sigma$  with  $d\lambda^{-1}/\sigma d\epsilon'$  in Fig. 3 are plotted. The red dash-dotted, black solid, pink long dashed, and forest green dashed lines show different models of the nonelastic cross sections of  $^{28}\text{Si}$  in Fig. 1. The reaction rate  $\lambda^{-1}$  of  $^{28}\text{Si}$  with  $E = 10^{20.5}$  eV can be obtained by integrating  $d\lambda^{-1}/d\epsilon'$  over photon energies  $\epsilon'$ .

### 3. Model dependence of cross sections of the GDRs

The GDR is the collective excitation of atomic nuclei, in which all protons and all neutrons oscillate out of phase. The GDR exhausts almost all of the total cross section of the dipole excitations. As it is a fundamental vibration mode of nuclei, GDR properties have been investigated for a long time and have served as an alternative observable correlated with other properties of nuclei. For example, the dipole polarizability, which can be evaluated from the cross section of dipole modes, has been applied for constraining the nuclear equation of state [34, 35, 36].

The approximate total cross section is calculated analytically, known as the Thomas-Reich-Kuhn sum rule value. However, the cross section distribution depends on the density functional, as shown in Fig. 1. This is because these density functionals have slightly different spin-isospin and momentum dependence. For instance, the energies of the peak cross section of  $^{28}\text{Si}$  listed in Table 2 have discrepancies of approximately 1 MeV, and they also deviate from the TALYS prediction. The discrepancy of the calculated peak energies and experimental one has been a long-standing problem that must be overcome, but it is difficult because there are not clear relations of the model parameters to the peak energy. Hence, it is important to see how these differences impact the UHECR.

Fig. 5 and Fig. 6 show the peak energies and cross sections of the GDRs, respectively. There are systematic differences between models; the RPA calculations with SkM\* and SLy4 tend to underestimate the peak energies and overestimate the peak cross sections than others in light nuclei. The mean free paths directly reflect the trend. Figure 7 shows mean free paths of  $^{28}\text{Si}$  obtained using the nonelastic cross sections in Fig. 1. The difference of the peak energies of the GDRs in Fig. 1 affects the Lorentz factors where the GDRs are the main channels in Fig. 7, and the difference of the peak cross sections in Fig. 1 affects the mean free paths in Fig. 7.

### 4. Model dependence of simulations of propagation of UHECRs

We fitted the experimental data of the Pierre Auger Observatory using TALYS and Skyrme-RPA with the method shown in Section 2 and obtained the fit parameters in Table 3. The explanations of the parameters are the followings.  $p$  shows the power index of the injection energy spectrum in Eq. (12),  $R_{\text{cut}}$  denotes the cutoff rigidity in Eq. (12), and  $m$  is the power

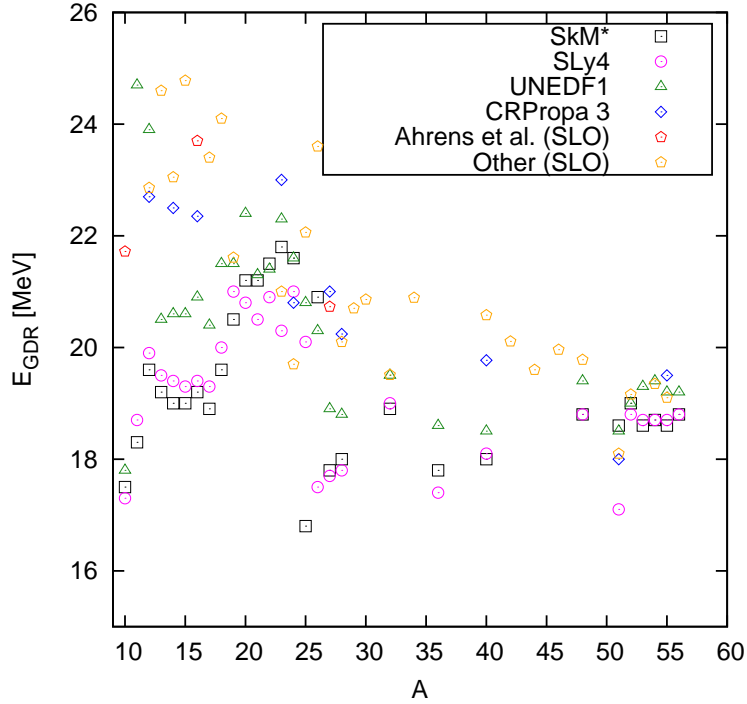


Figure 5: Model predictions of peak energies of the giant dipole resonances. Only the first peaks of the resonances with higher cross sections are plotted. The blue diamond shows the cross section used in CRPropa 3. The cross section is shown in Table 2 in [18]. The red and yellow hexagon show the standard Lorentzian model (SLO) of the experimental data in the IAEA library [9]. The photoabsorption cross sections were directly measured using accelerator facilities in Mainz for the red hexagons, and indirectly measured for the yellow hexagons.  $^{14}\text{C}$ ,  $^{40}\text{Ar}$  and  $^{48}\text{Ca}$  were not plotted to avoid mixing up with  $^{14}\text{N}$ ,  $^{40}\text{Ca}$  and  $^{48}\text{Ti}$ , respectively. Black square, pink circle, and forest green triangle show the cross sections obtained using the different density functionals in the RPA calculations.

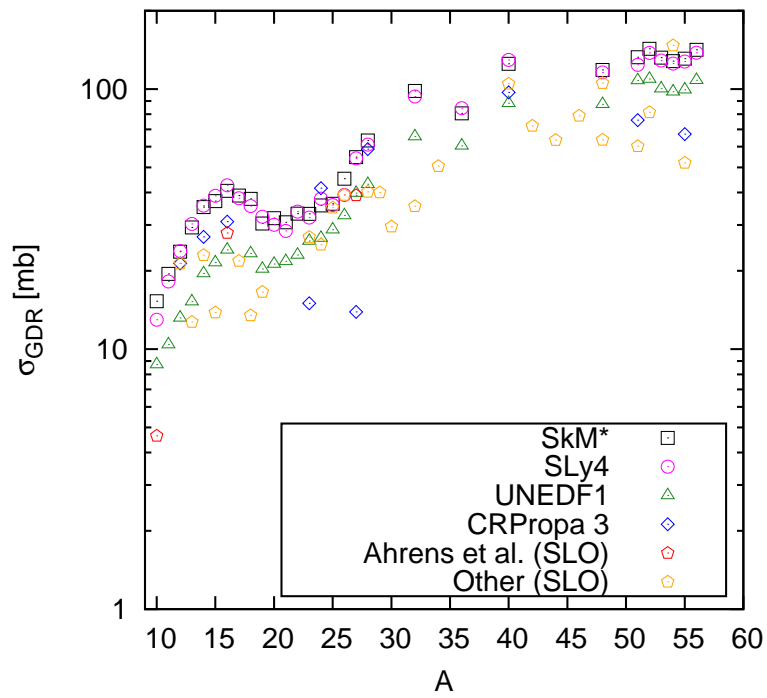


Figure 6: Model predictions of the photoabsorption cross sections of the giant dipole resonances at the peak energies in Fig. 5. The different point types are described in Fig. 5.

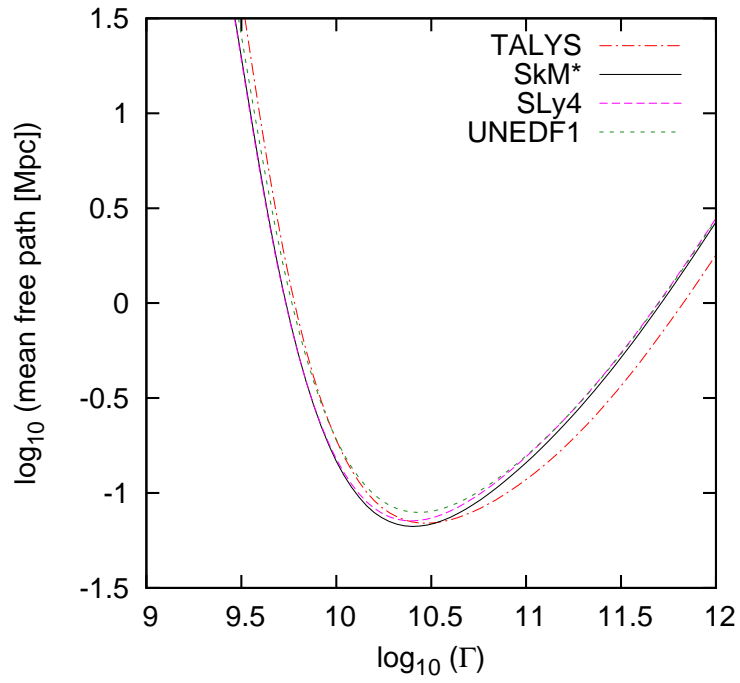


Figure 7: Model predictions of mean free paths using the cross sections of Fig. 1 with cosmic microwave background photons when redshift  $z = 0$ .  $\Gamma$  is a Lorentz factor of a  $^{28}\text{Si}$  nucleus.

index of the source evolution  $(1+z)^m$  per comoving unit volume. The shift of the energy scale of the model  $\Delta E/E$  is used when the simulated spectra and compositions at the energy  $(E + \Delta E)$  are compared with the data at the energy  $E$ , and  $f_A$  shows the fraction of the element at  $10^{18}$  eV in Eq. (12). As a result of the fittings, the experimental data can be reproduced with both TALYS and Skyrme-RPA. However, many of the fit parameters in Table 3 show significant differences between TALYS and Skyrme-RPA. The GDR peaks of Skyrme-RPA appear at lower energies than TALYS, and the difference in the GDR peaks mainly causes relatively soft UHECR spectra with Skyrme-RPA, as shown later in this section. In particular,  $f_A(^{28}\text{Si})$  and  $f_A(^{56}\text{Fe})$  of Skyrme-RPA are larger than TALYS to compensate the difference of the energy spectra in Table 3. The proton fraction  $f_A(^1\text{H})$  cannot be determined because of the limited contribution above  $10^{18.7}$  eV, so the proton fraction in Table 3 is fixed to be 0. The step sizes of  $p$ ,  $\log(R_{\text{cut}})$  and  $m$  are comparable to the uncertainties or smaller than those, so the errors of these parameters are not described in Table 3.

Fig. 8 and 9 show the comparison results of the energy spectra, which were calculated with TALYS and Skyrme-RPA using the same parameters in the column of TALYS in Table 3. We did not change the total number of simulated events between TALYS and Skyrme-RPA in these figures. The maximum difference of the energy spectra between TALYS and Skyrme-RPA is more than 20%. The difference is more than the statistical uncertainty of the experimental data, as shown in Fig. 9. We repeated the comparison of energy spectra when the RPA calculations of only one nucleus are applied to understand the contribution of which nucleus is important. Then, we searched the energy bins to find the maximum difference between TALYS and Skyrme-RPA in the spectral shape. Fig. 10 shows the maximum differences from default CRPropa in the spectral shape when the RPA calculations of only one nucleus are applied. The largest maximum difference from TALYS is obtained when the RPA calculations of  $^{28}\text{Si}$  are applied. The difference can be more than 5%, depending on the density functional. Fig. 11 shows the energy bins, showing the maximum difference in the spectral shape. The lighter nuclear species show the maximum difference at the lower energies because the Lorentz factors in the GDRs are relatively larger for lighter nuclei. We also fitted the normalization of the energy spectra with  $E > 10^{18.7}$  eV which were calculated with the RPA calculations in order to estimate the difference's impact on the interpretation in Fig. 12 and 13. The maximum difference of the energy spectra between TALYS and Skyrme-RPA can be



more than 20% which is more than the statistical uncertainty of the experimental data even if the normalization is adjusted. We compared the model predictions of  $\langle \ln A \rangle$  and  $\sigma^2(\ln A)$  in Fig. 14 and Fig. 15, respectively. The differences of  $\langle \ln A \rangle$  and  $\sigma^2(\ln A)$  between the models are smaller than the systematic uncertainty of the experimental data. Fig. 16, Fig. 17, and Fig. 18 show comparison between the data and models with their best-fit parameters in Table 3. The observed energy spectrum,  $\langle \ln A \rangle$ , and  $\sigma^2(\ln A)$  with  $E > 10^{18.7}$  eV are reproduced with Skyrme-RPA, as shown in these figures.

## 5. Conclusions and discussions

The PANDORA project finally plans to systematically measure photonuclear reactions from light to  $A \sim 60$  nuclei. Nuclear theories are needed to model the experimental data and estimate reactions that are not measured. The PANDORA project will start to measure the cross sections of a few nuclei in a few years. A reliable nuclear theory would also be informative in interpreting the current experimental data before various nuclei are newly measured. We studied the impact of the difference between TALYS and Skyrme-RPA in CRPropa on the interpretation of observations of UHECR nuclei. TALYS in CRPropa reflects the current experimental data. We found that the difference between TALYS and Skyrme-RPA of 29 stable nuclei in the spectral shape is more than 20% and larger than the statistical uncertainty of the observed UHECR energy spectrum when the same astrophysical parameters are assumed. The systematic model dependence of the GDR peaks was the biggest contribution to the difference. The biggest contribution is provided by  $^{28}\text{Si}$  in the spectral shape. The difference can be more than 5% if the model of  $^{28}\text{Si}$  is changed. The difference of best-fit astrophysical parameters obtained by a combined fit of UHECR energy spectrum and composition data can also be more than the uncertainty of the data between TALYS and Skyrme-RPA, as shown in Table 3. In the current situation, systematic uncertainties can exist in both theory and experiment, and it is difficult to conclude the source of the difference. The following things are considered to improve the RPA calculations and experimental data.

To improve the systematic model dependence of the GDR peaks, the density functional of the RPA calculations needs to be corrected because the density functional is not currently tuned to reproduce properties of excited states. The PANDORA project will experimentally test the model predictions of the peak energies and cross sections of the GDRs. Improv-

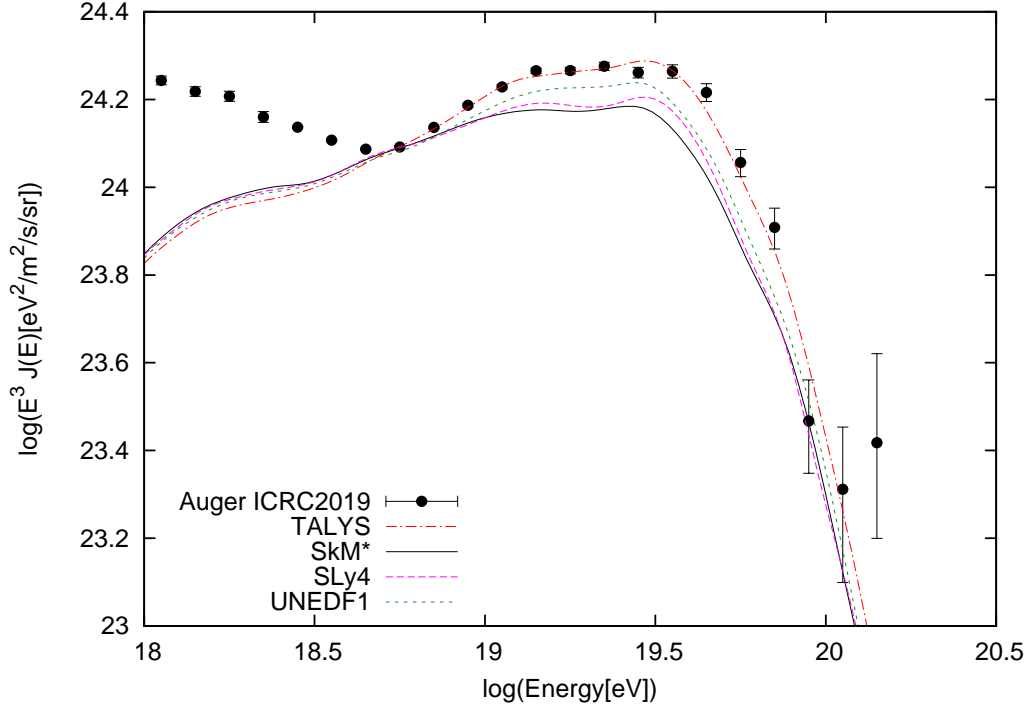


Figure 8: Comparison of simulated energy spectra and observed energy spectrum by the Pierre Auger Collaboration [37].  $J(E)$  denotes  $dN/dEdAd\Omega dt$  in  $\text{eV}^{-1}\text{m}^{-2}\text{s}^{-1}\text{sr}^{-1}$  where  $dN$  is number of cosmic rays with energies between  $E$  and  $E + dE$  which cross the area  $dA$  from the solid angle  $d\Omega$  during the time interval  $dt$ . 15 data points of the energy spectrum above  $10^{18.7}$  eV, 10 data points of  $\langle \ln A \rangle$  and 10 data points of  $\sigma^2(\ln A)$  were fitted with simulated results. We simulated energy spectra with different models using best-fit parameters of TALYS for comparison. The best-fit parameters are listed in the column of TALYS in Table 3. The black dots are observed energy spectrum. The red dash-dotted line is the energy spectrum simulated using TALYS. The black solid, pink long dashed, and forest green dashed lines are simulated with Skyrme-RPA using different density functionals.  $\chi^2$  values calculated using the red line and 15 data points with  $E > 10^{18.7}$  eV is 22.3. The black, pink, and forest green lines are inconsistent with the data.

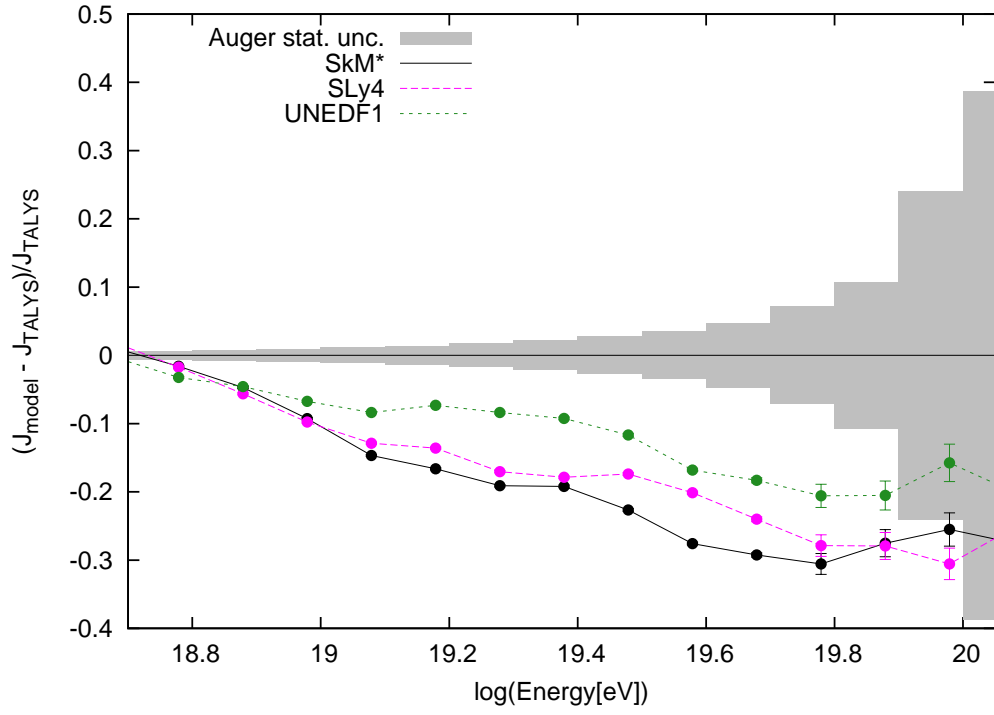


Figure 9: The relative differences of the energy spectra with the RPA calculations  $J_{\text{model}}$  from TALYS  $J_{\text{TALYS}}$  are plotted.  $J_{\text{model}}$  and  $J_{\text{TALYS}}$  are the same as Fig.8. The unit of  $J(E)$  is  $\text{eV}^{-1}\text{m}^{-2}\text{s}^{-1}\text{sr}^{-1}$ . The statistical uncertainties of the data are shown as the hatched region.

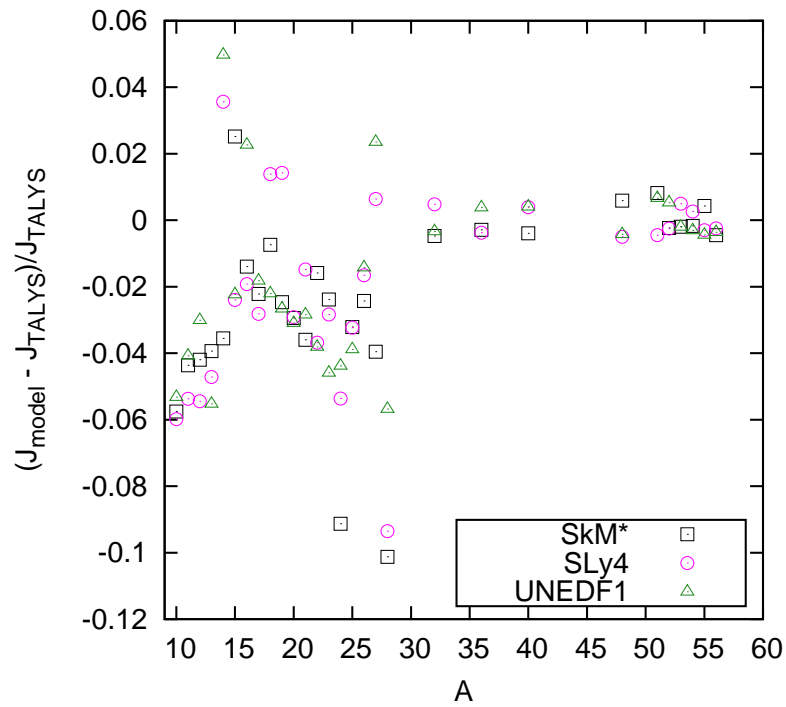


Figure 10: The vertical axis shows maximum differences from TALYS in the spectral shape when the RPA calculations of a nucleus with mass number  $A$  in the horizontal axis are applied.  $J_{\text{model}}$  and  $J_{\text{TALYS}}$  represent the same spectra as Fig. 9.

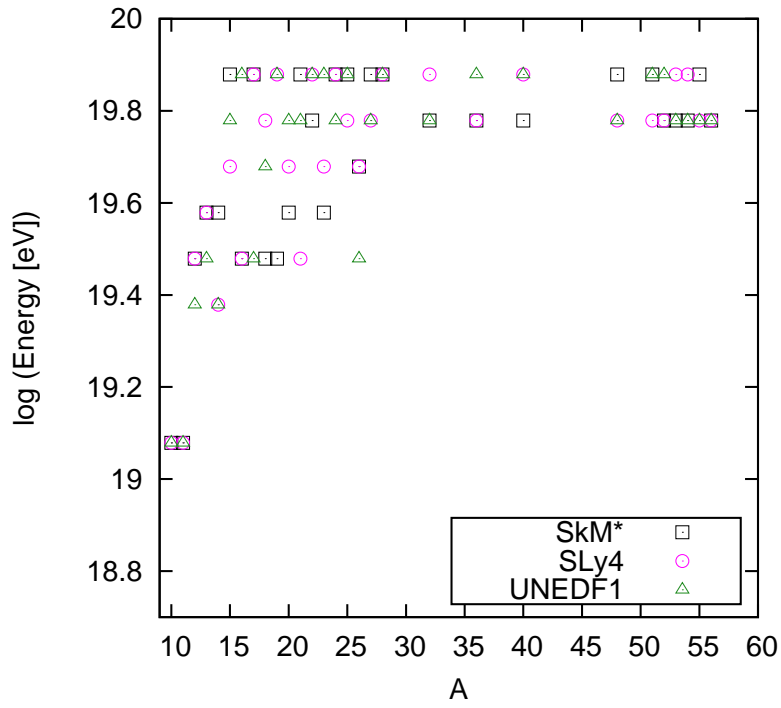


Figure 11: The vertical axis denotes energies that show the maximum difference in the spectral shape in Fig. 10. The step size of searched energies is 0.1 in  $\log(E/\text{eV})$ .  $E > 10^{19.9}$  eV is not searched because of the limited number of simulated events. The horizontal axis represents mass number  $A$ .

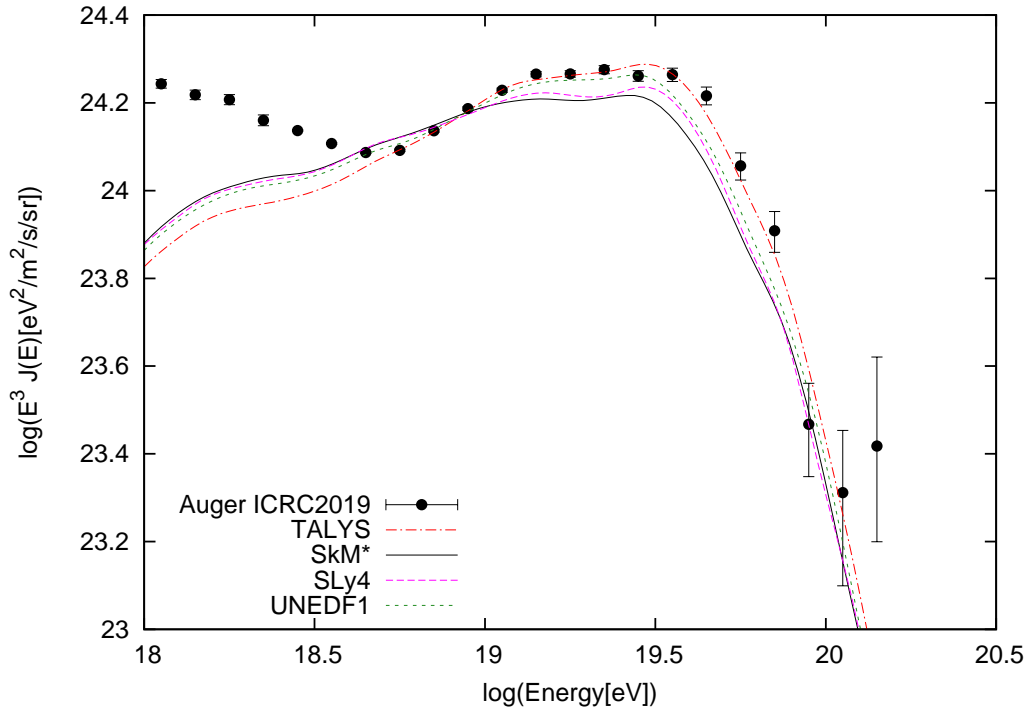


Figure 12: The same figure as Fig. 8 except for the normalizations of the black, pink, and forest green lines, obtained by fitting the data points with  $E > 10^{18.7}$  eV. The black solid, pink long dashed, and forest green dashed line are inconsistent with the data, and  $\chi^2$  values with these lines and the data points above  $10^{18.7}$  eV are 475, 355 and 108, respectively.

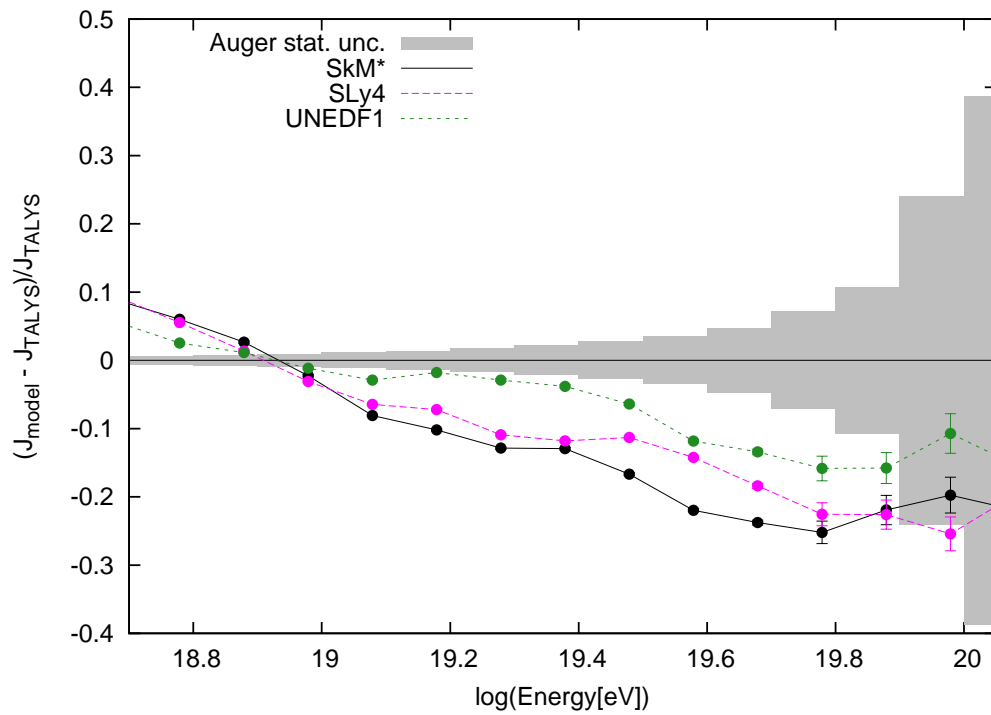


Figure 13: The same results as Fig. 12 are plotted here. In this figure, the relative differences of the model predictions of the intensities are plotted as Fig. 9.

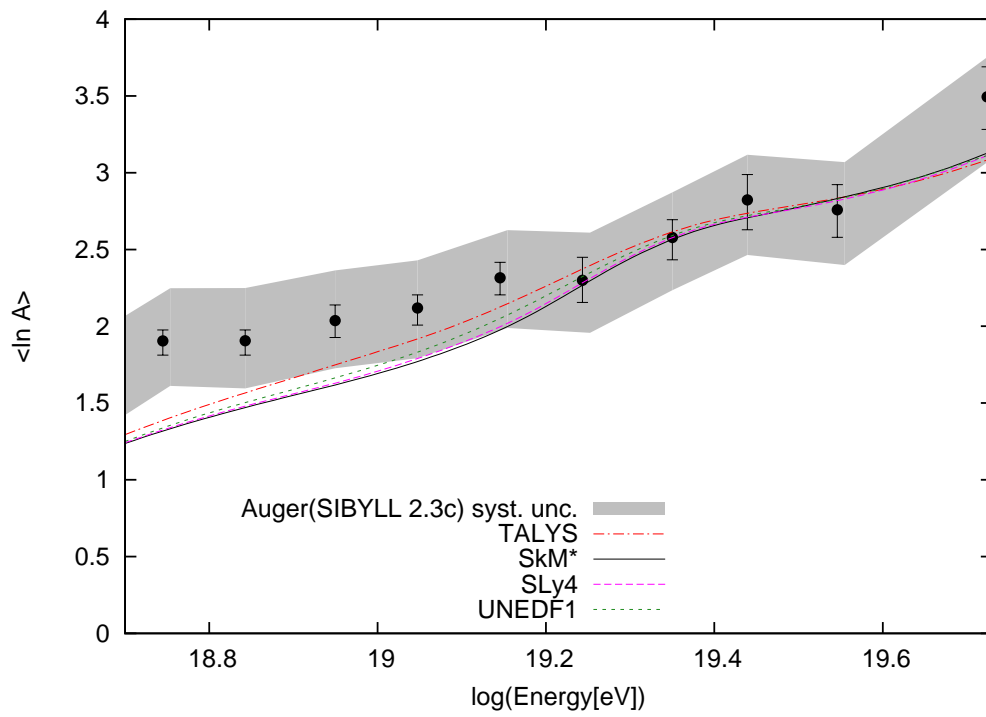


Figure 14: Comparison of simulated  $\langle \ln A \rangle$  of the same results as Fig.12.



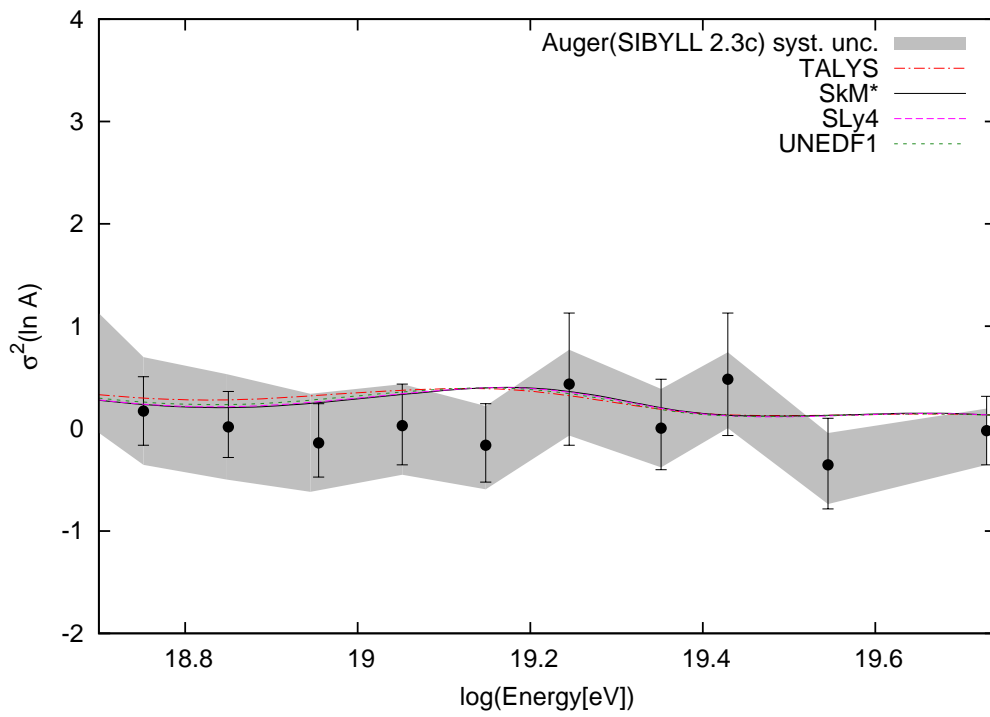


Figure 15: Comparison of simulated  $\sigma^2(\ln A)$  of the same results as Fig.12.

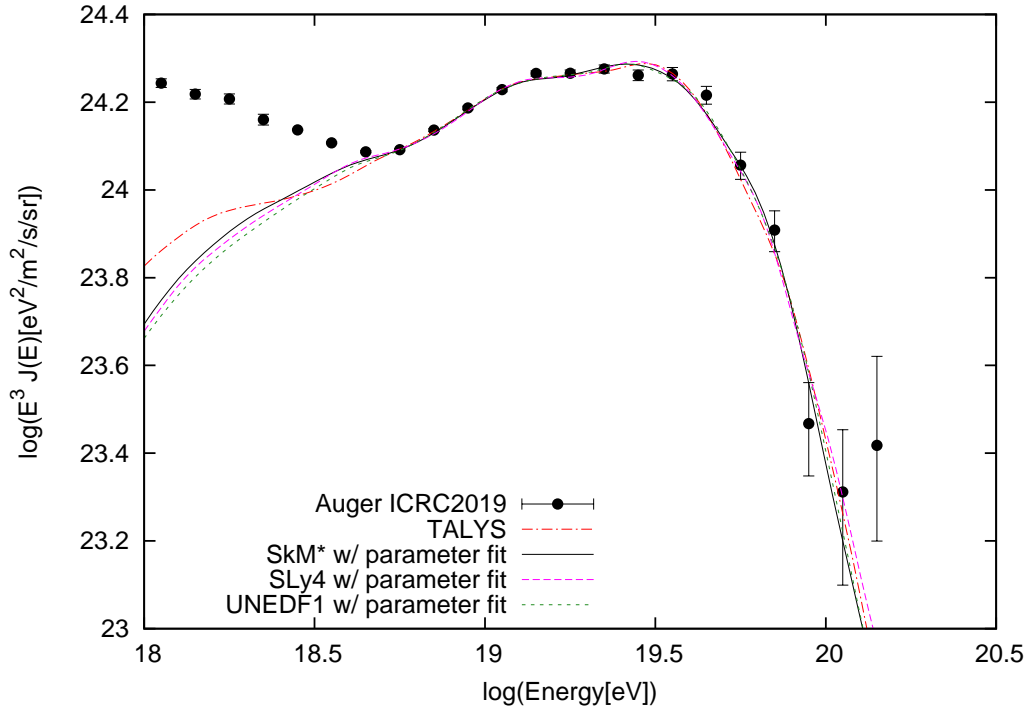


Figure 16: The data points and simulated energy spectrum with TALYS are the same as Fig. 12. The other plotted energy spectra were simulated using Skyrme-RPA with their best-fit astrophysical parameters. The parameters are listed in Table 3. The parameters were obtained by fitting the observed energy spectrum,  $\langle \ln A \rangle$  and  $\sigma^2(\ln A)$ .  $\chi^2$  values calculated using the black solid, pink long dashed, and forest green dashed line and the data with  $E > 10^{18.7}$  eV are 18, 29 and 16, respectively.

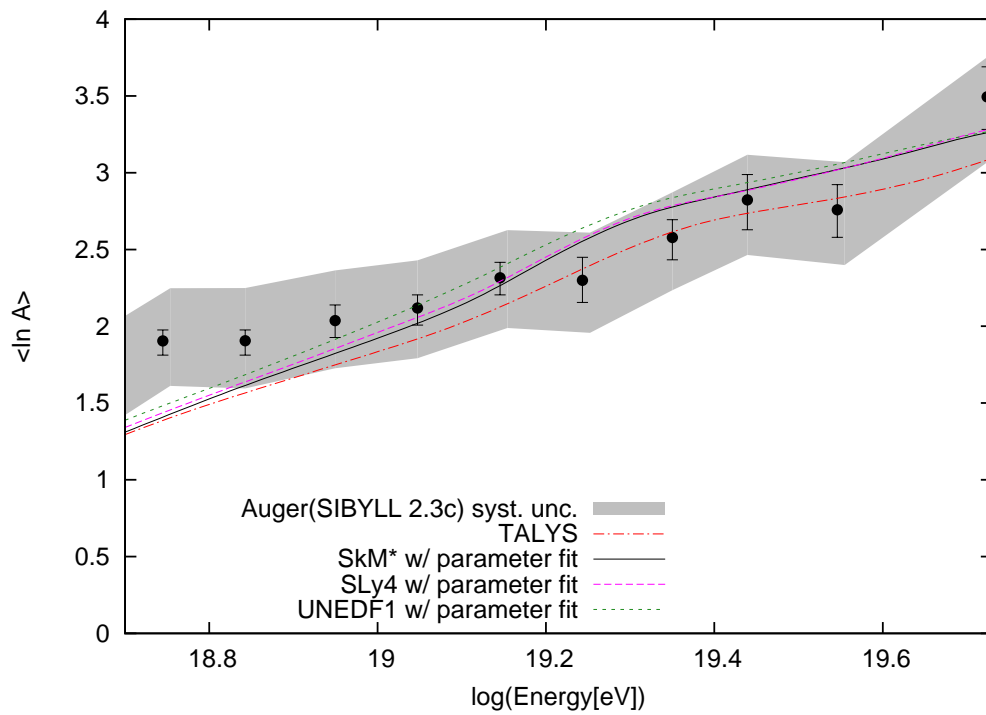


Figure 17: Comparison of simulated  $\langle \ln A \rangle$  of the same results as Fig.16.

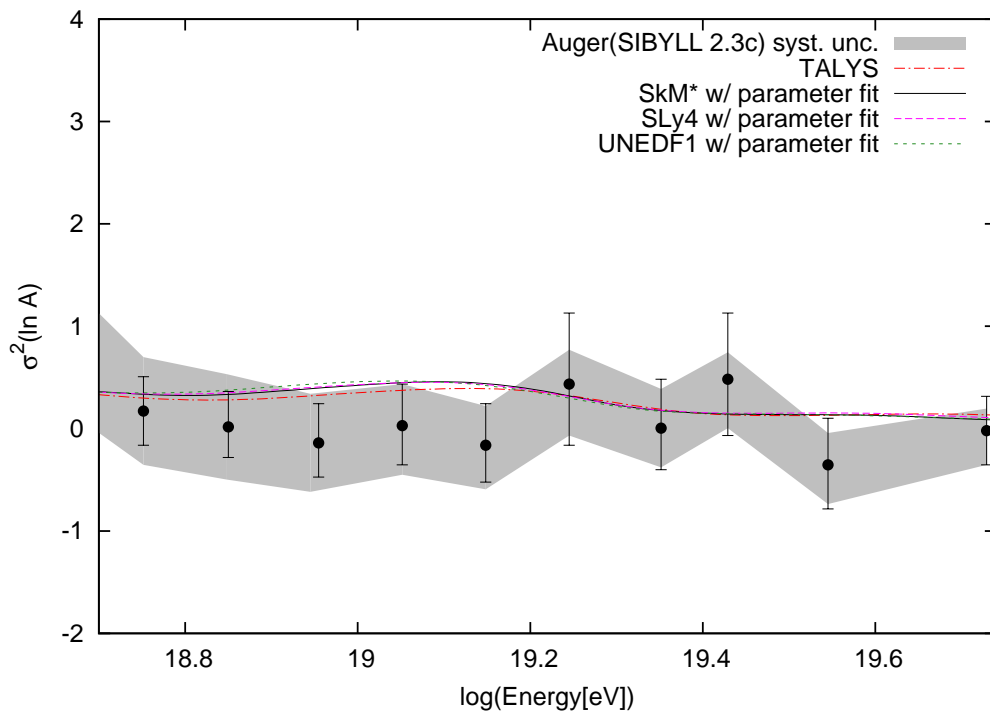


Figure 18: Comparison of simulated  $\sigma^2(\ln A)$  of the same results as Fig.16.

ing the Skyrme density functional model parameters is not straightforward because there is no one-to-one correspondence between each parameter and the GDR's peak energy and height. On the other hand, quite recently, the Monte Carlo calculation shows that some of the Skyrme parameters are correlated with the peak energy of the GDR [38]. The correlation would enable us to improve the Skyrme parameters. Therefore, we are planning to propose a new Skyrme parameter set that reproduces the experimental data of  $E1$  strength and gives more reliable  $E1$  strength of nuclei in which there are no experimental data in the near future. There were systematic discrepancies in the cross sections between experimental facilities in the past. The PANDORA project plans to solve such systematic uncertainty using modern experimental methods at three independent facilities.

### Acknowledgement

This work is supported by by the Pioneering Program of RIKEN for Evolution of Matter in the Universe (r-EMU). This work was supported by JSPS KAKENHI (A) Grant Number JP19H00693. We are thankful to members of the PANDORA project for fruitful discussions. The simulations in this work were partially obtained using HOKUSAI supercomputer at RIKEN. E.K. and S.N. thank supports from "Pioneering Program of RIKEN for Evolution of Matter in the Universe (r-EMU)". We are also thankful to Donald Warren III for many corrections of the sentences.

### References

- [1] A. Aab et al. (The Pierre Auger Collaboration), The Pierre Auger Cosmic Ray Observatory, Nuclear Instruments and Methods in Physics Research Section A 798 (21) (2015) 172–213. doi:10.1016/j.nima.2015.06.058.
- [2] A. Aab et al. (The Pierre Auger Collaboration), Depth of maximum of air-shower profiles at the Pierre Auger Observatory. I. Measurements at energies above  $10^{17.8}$  eV, Physical Review D 90 (2014) 122005. doi:10.1103/PhysRevD.90.122005.
- [3] A. Aab et al. (The Pierre Auger Collaboration), Depth of maximum of air-shower profiles at the Pierre Auger Observatory. II.

Composition implications, *Physical Review D* 90 (2014) 122006. doi:10.1103/PhysRevD.90.122006.

- [4] A. Aab et al. (The Pierre Auger Collaboration), Observation of a large-scale anisotropy in the arrival directions of cosmic rays above  $8 \times 10^{18}$  eV, *Science* 357 (6357) (2017) 1266–1270. doi:10.1126/science.aan4338.
- [5] A. Aab et al. (The Pierre Auger Collaboration), An Indication of Anisotropy in Arrival Directions of Ultra-high-energy Cosmic Rays through Comparison to the Flux Pattern of Extragalactic Gamma-Ray Sources, *The Astrophysical Journal Letters* 853 (2) (2018) L29. doi:10.3847/2041-8213/aaa66d.
- [6] Armando di Matteo, Luis Anchordoqui, Teresa Bister, Jonathan Biteau, Lorenzo Caccianiga, Rogério de Almeida, Olivier Deligny, Ugo Giaccari, Diego Harari, Jihyun Kim, Mikhail Kuznetsov, Ioana Maris, Grigory Rubtsov, Peter Tinyakov, Sergey Troitsky, Federico Urban on behalf of the Pierre Auger and the Telescope Array Collaboration, UHECR arrival directions in the latest data from the original Auger and TA surface detectors and nearby galaxies, in: *37th International Cosmic Ray Conference (ICRC 2021)*, 2021, PoS(ICRC2021)308.
- [7] T. Abu-Zayyad et al., The surface detector array of the Telescope Array experiment, *Nuclear Instruments and Methods in Physics Research Section A* 689 (11) (2012) 87–97. doi:10.1016/j.nima.2012.05.079.
- [8] D. Allard, M. Ave1, N. Busca, M. Malkan, A. Olinto, E. Parizot, F. Stecker, T. Yamamoto, Cosmogenic Neutrinos from the propagation of Ultra High Energy Nuclei, *Journal of Cosmology and Astroparticle Physics* 09 (2006) 005. doi:10.1088/1475-7516/2006/09/005.
- [9] T. Kawano, Y. Cho, P. Dimitriou, D. Filipescu, N. Iwamoto, V. Plujko, X. Tao, H. Utsunomiya, V. Varlamov, R. Xu, R. Capote, I. Gheorghe, O. Gorbachenko, Y. Jin, T. Renstrøm, K. Stopani, Y. Tian, G. Tveten, J. Wang, T. Belgya, R. Firestone, S. Goriely, J. Kopecky, M. Krtička, R. Schwengner, S. Siem, M. Wiedeking, IAEA Photoneuclear Data Library 2019, *Nuclear Data Sheets* 163 (2020) 109–162. doi:10.1016/j.nds.2019.12.002.

- [10] D. Boncioli, A. Fedynitch, W. Winter, Nuclear Physics Meets the Sources of the Ultra-High Energy Cosmic Rays, *Scientific Reports* 7 (2017) 4882. doi:10.1038/s41598-017-05120-7.
- [11] Atsushi Tamii, PANDORA project: measurement of nuclear photodisintegrations for extragalactic propagation of UHECRs, in: *XSCRC 2019 Workshop*, 2019.
- [12] The PANDORA Collaboration, PANDORA project: photo-nuclear reaction below a mass of  $A=60$ , *European Physical Journal A*, in preparation.
- [13] P. von Neumann-Cosel, A. Tamii, Electric and magnetic dipole modes in high-resolution inelastic proton scattering at  $0^\circ$ , *The European Physical Journal A* 55 (7) (2019) 1–52.
- [14] S. Gales et al., The extreme light infrastructure—nuclear physics (ELI-NP) facility: new horizons in physics with 10 PW ultra-intense lasers and 20 MeV brilliant gamma beams, *Reports on Progress in Physics* 81 (9) (2018) 094301.
- [15] J. Puget, F. Stecker, J. Bredekamp, Photonuclear interactions of ultrahigh energy cosmic rays and their astrophysical consequences, *The Astrophysical Journal* 205 (1976) 638. doi:doi:10.1086/154321.
- [16] E. Khan, S. Goriely, D. Allard, E.Parizot, T.Suomijärvia, A.J.Koning, S.Hilaire, M.C.Duijvestijn, Photodisintegration of ultra-high-energy cosmic rays revisited, *Astroparticle Physics* 23 (2) (2005) 191–201. doi:10.1016/j.astropartphys.2004.12.007.
- [17] A. J. Koning, S. Hilaire, M. C. Duijvestijn, TALYS: Comprehensive Nuclear Reaction Modeling, *AIP Conference Proceedings* 769 (2005) 1154. doi:10.1063/1.1945212.
- [18] R. A. Batista, A. Dundovic, M. Erdmann, K.-H. Kampert, D. Kuempel, G. Müller, G. Sigl, A. van Vliet, D. Walz, T. Winchen, CRPropa 3—a public astrophysical simulation framework for propagating extraterrestrial ultra-high energy particles, *Journal of Cosmology and Astroparticle Physics* 05 (2016) 038. doi:10.1088/1475-7516/2016/05/038.

- [19] R. Aloisio, D. Boncioli, A. di Matteo, A. F. Grillo, S. Petrera, F. Salamida, SimProp v2r4: Monte Carlo simulation code for UHECR propagation, *Journal of Cosmology and Astroparticle Physics* 11 (2017) 009. doi:10.1088/1475-7516/2017/11/009.
- [20] J. Heinze, A. Fedynitch, D. Boncioli, W. Winter, A New View on Auger Data and Cosmogenic Neutrinos in Light of Different Nuclear Disintegration and Air-shower Models, *The Astrophysical Journal* 873 (2019) 88. doi:10.3847/1538-4357/ab05ce.
- [21] T. Inakura, T. Nakatsukasa, K. Yabana, Self-consistent calculation of nuclear photoabsorption cross sections: Finite amplitude method with Skyrme functionals in the three-dimensional real space, *Physical Review C* 80 (2009) 044301. doi:10.1103/PhysRevC.80.044301.
- [22] T. Inakura, T. Nakatsukasa, K. Yabana, Emergence of pygmy dipole resonances: Magic numbers and neutron skins, *Physical Review C* 84 (2011) 021302(R). doi:10.1103/PhysRevC.84.021302.
- [23] P. Ring, P. Schuck, *The Nuclear Many-Body Problem*, Springer-Verlag, 1980.
- [24] T. Nakatsukasa, K. Matsuyanagi, M. Matsuo, K. Yabana, Time-dependent density-functional description of nuclear dynamics, *Review of Modern Physics* 88 (2016) 045004.
- [25] J. Bartel, P. Quentin, M. Brack, C. Guet, H.-B. Håkansson, Towards a better parametrisation of Skyrme-like effective forces: A critical study of the SkM force, *Nuclear Physics A* 386 (1) (1982) 79–100. doi:10.1016/0375-9474(82)90403-1.
- [26] E. Chabanat, P. Bonche, P. Haensel, J. Meyer, R. Schaeffer, A Skyrme parametrization from subnuclear to neutron star densities, *Nuclear Physics A* 627 (4) (1997) 710–746. doi:10.1063/1.1945212.
- [27] M. Kortelainen, J. McDonnell, W. Nazarewicz, P.-G. Reinhard, J. Sarich, N. Schunck, M. Stoitsov, S. Wild, Nuclear energy density optimization: Large deformations, *Physical Review C* 85 (2012) 024304. doi:10.1103/PhysRevC.85.024304.



- [28] A. Akmal, V. R. Pandharipande, D. G. Ravenhall, Equation of state of nucleon matter and neutron star structure, *Physical Review C* 58 (1998) 1804–1828. doi:10.1103/PhysRevC.58.1804. URL <https://link.aps.org/doi/10.1103/PhysRevC.58.1804>
- [29] M. Beiner, H. Flocard, N. V. Giai, P. Quentin, Nuclear ground-state properties and self-consistent calculations with the skyrme interaction, *Nuclear Physics A* 238 (1975) 26–69. doi:10.1016/0375-9474(75)90338-3.
- [30] F. Stecker, M. Salamon, Photodisintegration of Ultra-High-Energy Cosmic Rays: A New Determination, *The Astrophysical Journal* 512 (2) (1999) 521–526. doi:10.1086/306816.
- [31] R. C. Gilmore, R. S. Somerville, J. R. Primack, A. Domínguez, Semi-analytic modelling of the extragalactic background light and consequences for extragalactic gamma-ray spectra, *Physical Review C* 422 (4) (2012) 3189–3207. doi:10.1111/j.1365-2966.2012.20841.x.
- [32] F. Riehn, H. P. Dembinski, R. Engel, A. Fedynitch, T. K. Gaisser, T. Stanev, The hadronic interaction model SIBYLL 2.3c and Feynman scaling. URL <https://arxiv.org/abs/1709.07227>
- [33] A. Aab et al. (The Pierre Auger Collaboration), Combined fit of spectrum and composition data as measured by the Pierre Auger Observatory, *Journal of Cosmology and Astroparticle Physics* 04 (2017) 38. doi:10.1088/1475-7516/2017/04/038.
- [34] X. Roca-Maza, M. Brenna, G. Colò, M. Centelles, X. Viñas, B. K. Agrawal, N. Paar, D. Vretenar, J. Piekarewicz, Electric dipole polarizability in 208pb: Insights from the droplet model, *Physical Review C* 88 (2013) 024316.
- [35] A. Tamii, P. von Neumann-Cosel, I. Poltoratska, Electric dipole response of 208pb from proton inelastic scattering: Constraints on neutron skin thickness and symmetry energy, *European Physical Journal A* 50 (2014) 28. doi:10.1140/epja/i2014-14028-7.
- [36] T. Inakura, H. Nakada, Constraining the slope parameter of the symmetry energy from nuclear structure, *Physical Review C* 92 (2015) 064302.

- [37] A. Aab et al. (The Pierre Auger Collaboration), Measurement of the cosmic-ray energy spectrum above  $2.5 \times 10^{18}$  eV using the Pierre Auger Observatory, *Physical Review D* 102 (2020) 062005. doi:10.1103/PhysRevD.102.062005.
- [38] T. Inakura, Uncertainty evaluation of peak energy of giant dipole resonance propagated from uncertainties of skyrme parametersarXiv:2205.12671.

Table 1: Separation energies of nuclei in MeV

Nuclear Species	SkM*	SLy4	UNEDF1
<sup>10</sup> B	11.2	10.5	9.5
<sup>11</sup> B	13.7	13.4	11.5
<sup>12</sup> C	14.1	14.1	12.3
<sup>13</sup> C	8.7	9.5	8.3
<sup>14</sup> N	8.2	9.1	8.4
<sup>15</sup> N	10.3	11.5	10.7
<sup>16</sup> O	10.3	11.2	10.1
<sup>17</sup> O	7.4	6.7	6.0
<sup>18</sup> O	7.7	7.2	5.9
<sup>19</sup> F	9.1	9.2	9.0
<sup>20</sup> Ne	9.2	9.3	8.4
<sup>21</sup> Ne	10.8	10.6	9.8
<sup>22</sup> Ne	11.0	10.7	9.2
<sup>23</sup> Na	10.0	9.9	9.6
<sup>24</sup> Mg	9.5	9.4	8.6
<sup>25</sup> Mg	10.6	10.1	9.5
<sup>26</sup> Mg	11.3	11.0	9.9
<sup>27</sup> Al	10.5	10.5	10.1
<sup>28</sup> Si	10.3	10.5	9.5
<sup>32</sup> S	7.3	7.4	6.6
<sup>36</sup> Ar	6.4	7.4	6.8
<sup>40</sup> Ca	7.5	8.4	7.6
<sup>48</sup> Ti	9.5	9.7	9.5
<sup>52</sup> Cr	9.0	9.1	8.9
<sup>56</sup> Fe	8.8	8.9	8.5

Table 2: Peak energy of calculated cross section of <sup>28</sup>Si in MeV

SkM*	SLy4	UNEDF1
18.0	17.8	18.9

Table 3: Fit parameters

Fit parameter	TALYS	SkM*
$p$	-1.8	-1.1
$R_{\text{cut}}$ (V)	$10^{18.1}$	$10^{18.2}$
$m$ (evolution parameter)	2	0
Shift of the energy scale of the model $\Delta E/E$ (%)	$6.8 \pm 1.0$	$-7.8 \pm 0.9$
$f_A$ ( $^1\text{H}$ ) (%)	0	0
$f_A$ ( $^4\text{He}$ ) (%)	$97.7 \pm 0.2$	$95.4 \pm 0.4$
$f_A$ ( $^{14}\text{N}$ ) (%)	$2.3 \pm 0.2$	$4.2^{+0.4}_{-0.3}$
$f_A$ ( $^{28}\text{Si}$ ) (%)	$(5.1^{+0.7}_{-0.6}) \cdot 10^{-2}$	$(3.6^{+0.5}_{-0.4}) \cdot 10^{-1}$
$f_A$ ( $^{56}\text{Fe}$ ) (%)	$(3.7^{+1.0}_{-0.8}) \cdot 10^{-4}$	$(3.4 \pm 0.4) \cdot 10^{-3}$

Fit parameter	SLy4	UNEDF1
$p$	-1.0	-0.9
$R_{\text{cut}}$ (V)	$10^{18.2}$	$10^{18.2}$
$m$ (evolution parameter)	0	0
Shift of the energy scale of the model $\Delta E/E$ (%)	$-6.5 \pm 1.2$	$-6.7 \pm 1.4$
$f_A$ ( $^1\text{H}$ ) (%)	0	0
$f_A$ ( $^4\text{He}$ ) (%)	$95.4^{+0.5}_{-0.4}$	$96.6^{+0.4}_{-0.3}$
$f_A$ ( $^{14}\text{N}$ ) (%)	$4.2^{+0.5}_{-0.4}$	$3.0 \pm 0.3$
$f_A$ ( $^{28}\text{Si}$ ) (%)	$(3.3 \pm 0.5) \cdot 10^{-1}$	$(3.3 \pm 0.5) \cdot 10^{-1}$
$f_A$ ( $^{56}\text{Fe}$ ) (%)	$(5.3 \pm 0.2) \cdot 10^{-3}$	$(4.3^{+0.2}_{-0.1}) \cdot 10^{-3}$